American Mineralogist, Volume 104, pages 73–78, 2019

Minerals in cement chemistry: A single-crystal neutron diffraction study of ettringite, $Ca_6Al_2(SO_4)_3(OH)_{12}\cdot 27H_2O$

G. Diego Gatta[1,2,*], Ulf Hålenius[3], Ferdinando Bosi[4], Laura Cañadillas-Delgado[5,6], and Maria Teresa Fernandez-Diaz[5]

[1]Dipartimento di Scienze della Terra, Università degli Studi di Milano, Via Botticelli 23, I-20133 Milano, Italy; ORCID 0000-0001-8348-7181
[2]CNR-Istituto di Cristallografia, Via Amendola 122/O, I-70126 Bari, Italy
[3]Department of Geosciences Swedish Museum of Natural History, P.O. Box 50 007, SE-104 05 Stockholm, Sweden
[4]Department of Earth Sciences, Sapienza University di Rome, Piazzale A. Moro 5, I-00185, Roma, Italy
[5]Institut Laue-Langevin, 71 Avenue des Martyrs, F-38042 Grenoble, France
[6]Centro Universitario de la Defensa de Zaragoza, ctra Huesca s/n, 50090 Zaragoza, Spain

Abstract

Ettringite, reported with ideal formula $Ca_6Al_2(SO_4)_3(OH)_{12}\cdot 26H_2O$, is recognized as a secondary-alteration mineral and as an important crystalline constituent of Portland cements, playing different roles at different time scales. It contains more than 40 wt% of H_2O. The crystal structure and crystal chemistry of ettringite were investigated by electron microprobe analysis in wavelength-dispersive mode, infrared spectroscopy, and single-crystal neutron diffraction at 20 K. The anisotropic neutron structure refinement allowed the location of (22+2) independent H sites, the description of their anisotropic vibrational regime and the complex hydrogen-bonding schemes. Analysis of the difference-Fourier maps of the nuclear density showed a disordered distribution of the inter-column ("free") H_2O molecules of the ettringite structure, modeled (in the structure refinement) with two independent and mutually exclusive configurations. As the disorder is still preserved down to 20 K, we are inclined to consider that as a "static disorder." The structure of ettringite is largely held together by hydrogen bonding: the building units [i.e., SO_4 tetrahedra, $Al(OH)_6$ octahedra, and $Ca(OH)_4(H_2O)_4$ polyhedra] are interconnected through an extensive network of hydrogen bonds. The ettringite of this study has ideal composition $Ca_6Al_2(SO_4)_3(OH)_{12}\cdot 27H_2O$, with (Mn+Fe+Si+Ti+Na+Ba) < 0.04 atoms per formula unit. The effect of the low-temperature stability of ettringite and thaumasite on the pronounced "Sulfate Attack" of Portland cements, observed in cold regions, is discussed.

Keywords: Ettringite, Portland cement, crystal chemistry, single-crystal neutron diffraction, infrared spectroscopy, hydrogen bonding

Introduction

Ettringite, with ideal chemical formula reported in the literature $Ca_6Al_2(SO_4)_3(OH)_{12}\cdot 26H_2O$ [$a \sim 11.2$ Å, $c \sim 21.3$ Å, space group $P31c$, or $P6_3/mcm$, $Z = 2$], occurs in metamorphosed limestone (near igneous contacts or in xenoliths) or as a low-temperature secondary-alteration phase (e.g., weathering crusts on larnite rocks), usually associated with portlandite, afwillite, hydrocalumite, mayenite, and gypsum. It is expected to form a solid solution with thaumasite, $Ca_3Si(OH)_6(CO_3)(SO_4)\cdot 12H_2O$ (Moore and Taylor 1970; Barnett et al. 2000).

More than in nature, an ettringite-like phase is an important crystalline constituent of the Portland cement, and it plays different roles at different time scales. In early hydration stages, the crystallization of ettringite governs the set rate of the calcium aluminate phase ("C3A", $Ca_3Al_2O_6$), which is highly reactive (Taylor 1997; Renaudin et al. 2007). In aged cement, delayed formation of ettringite and thaumasite can promote destructive processes, especially in cement products in which limestone is used as a filling material (Hartshorn et al. 1999) and a diffusion of sulfate-rich fluids occurs (e.g., by contact with sulfate-rich soils or groundwater) (Crammond 1985). The main cement hydration products, i.e., calcium silicate or aluminate hydrates (the so-called C-S-H and C-A-H) and calcium hydroxide [portlandite $Ca(OH)_2$], are decomposed as a result of both sulfate attack and carbonation: as C-S-H and C-A-H provide most of the binding strength, the formation of ettringite and thaumasite leads to weakening and disintegration of the cement matrix. This phenomenon is more pronounced in cement structures below ground (e.g., Hartshorn et al. 1999; Bensted 1999; Hobbs and Taylor 2000; Santhanam et al. 2001; Zhang et al. 2009; Gatta et al. 2012). The effect of carbonate ions on delayed ettringite formation was recently reported by Asamoto et al. (2017).

The crystalline structure of ettringite has been previously investigated by several authors by single-crystal or powder X-ray diffraction (e.g., Moore and Taylor 1968, 1970; Goetz-Neunhoeffer and Neubauer 2006) and by neutron powder diffraction (Hartman and Berliner 2006). Its crystal structure is significantly complex (Fig. 1): it consists of $[Ca_3[Al(OH)_6]\cdot 12H_2O]$ columns, parallel to [001], and connected by sulfate groups via hydrogen bonds with H_2O molecules. In each column, $Al(OH)_6$-octahedra alternate with triplets of calcium polyhedra with coordination number CN = 8, i.e., coordinated by four (OH)-groups and four H_2O molecules

* E-mail: diego.gatta@unimi.it

0003-004X/19/0001–073$05.00/DOI: https://doi.org/10.2138/am-2019-6783

disposed around the threefold axis. Disordered distribution affecting the inter-column H_2O molecules was reported, and even the disordered distribution of the building groups would lead to a different symmetry of the structure (Moore and Taylor 1970). The structure of a synthetic ettringite-type compound, $Ca_6[Al(OD)_6]_2(SO_4)_3 \cdot 25.5D_2O$, was re-investigated by Hartman and Berliner (2006) by neutron powder diffraction. The authors were able to locate the proton sites with a structure model in the space group $P31c$. However, all the sites were modeled isotropically, with unusually different displacement factors for atoms of the same ionic groups, and some of the refined site occupancy factors showing partial occupancies.

The aforementioned studies, along with those conducted on the thermal and compressional behavior of ettringite (e.g., Skoblinskaya and Krasilnikov 1975; Skoblinskaya et al. 1975; Zhou and Glasser 2001; Deb et al. 2003; Hartman et al. 2006;

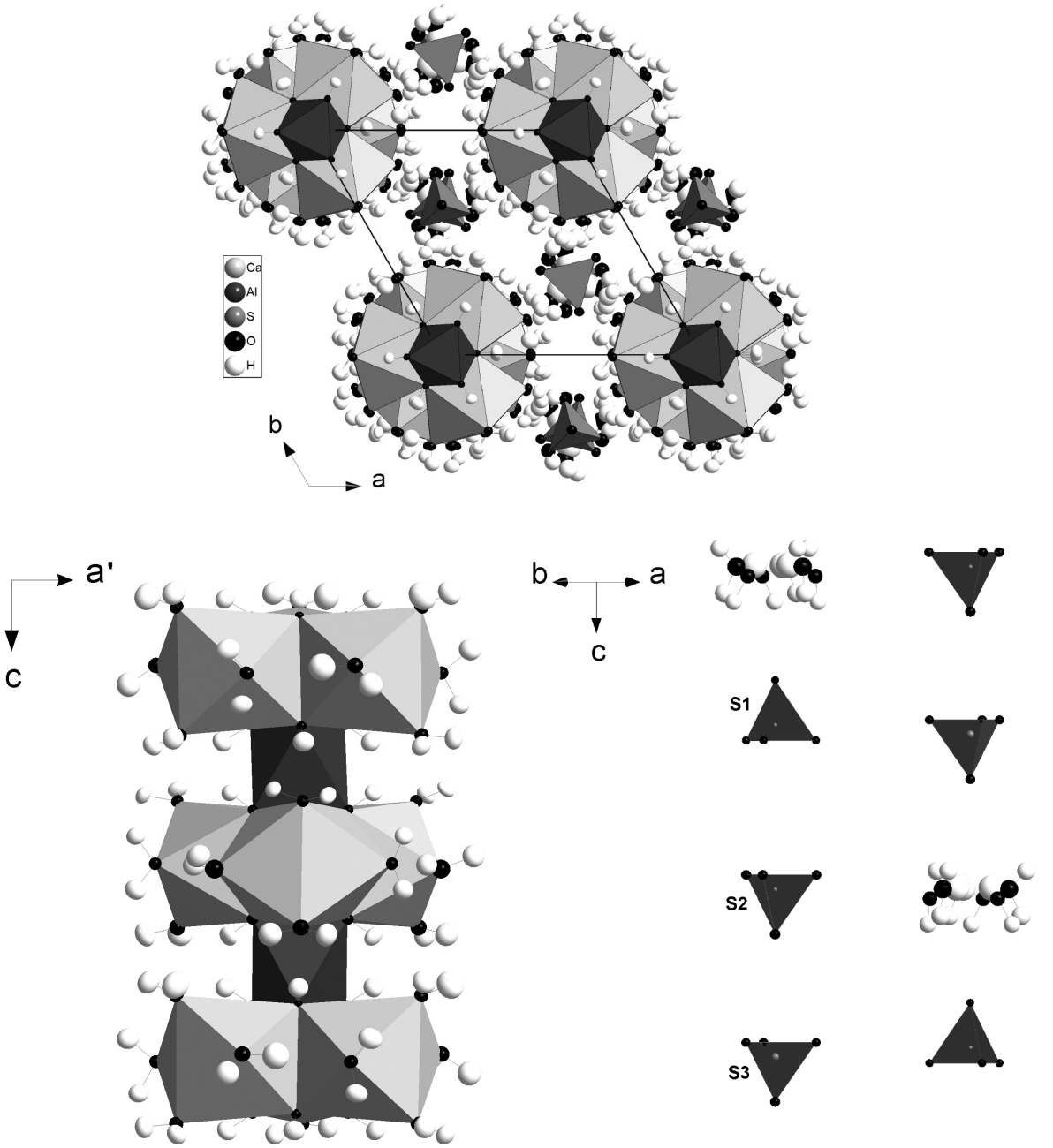

FIGURE 1. (**top**) The crystal structure of ettringite viewed down [001] based on the neutron structure refinement at 20 K of this study. Displacement-ellipsoid probability factor: 50%. (**bottom**) The configuration of the $[Ca_3Al(OH)_6(H_2O)_{12}]$ building-block units forming columns parallel to [001] (**left**) and of the alternating H_2O and SO_4 tetrahedra running along [001] (**right**).

Speziale et al. 2008; Renaudin et al. 2010; Manzano et al. 2012), suggest that: (1) the hydrogen bonds play an important role in the structural stability of ettringite, but clarification of this role is obscured by the difficulties in locating the protons and thence of refining the bond distances (i.e., O-H) and angles (i.e., O-H···O), and (2) inter-column H_2O could be disordered, but it is still unclear the nature of the disorder (static or dynamic?) and why the H_2O content is found to vary between 24 and 26 molecules per formula unit (pfu) (Manzano et al. 2012). In the framework of a long-term project on the sulfate compounds occurring in cements, we have previously described the mechanisms (at the atomic scale) that stabilize the thaumasite structure at low temperature, giving a clue about the reason of the pronounced sulfate attack of Portland cements observed in cold regions (Gatta et al. 2012). To extend our investigations on the second most important compound, which governs the low-*T* sulfate attack in cements, the aim of the present study is a re-investigation of the crystal structure and crystal chemistry of a natural ettringite at low-*T* by means of single-crystal neutron diffraction, infrared spectroscopy, and electron microprobe analysis in wavelength-dispersive mode, to define: (1) the reliable location of all the proton sites and the real topological configuration of the H_2O and (OH) groups, for a full description of the atomic relationship via the hydrogen-bonds; (2) the anisotropic displacement parameters of the H-sites; and (3) the nature of the disordered distribution of the H_2O molecules into structure, and its potential role on the stability of ettringite.

Experimental methods

The sample description used in this study, along with the characterization protocols by electron microprobe analysis in wavelength-dispersive mode, powder infrared spectroscopy, and anisotropic structure refinement, based on single-crystal neutron diffraction data collected at 20 K, are reported in a section of the Supplementary Materials[1].

Sample characterization

Ettringite was separate from a specimen from the N'Chwaning mine, Kuruman, Cape Province, Republic of South Africa. The sample (NRM 19950132) is deposited in the mineral collections at the Swedish Museum of Natural History. Large (up to 1.5 cm in length) prismatic, yellow crystals of ettringite and large (up to 1 cm), euhedral, black crystals of braunite-2Q are set on a matrix of fine- to medium-sized (up to 1 mm), pale-red, granular grains of andradite and fine-grained clinochlore.

Electron microprobe analyses were obtained by wavelength-dispersive spectroscopy (EPMA–WDS) with a Cameca SX50 instrument at the "Istituto di Geologia Ambientale e Geoingegneria, CNR" of Rome, Italy, using the following analytical conditions: accelerating voltage 15 kV, beam current 15 nA, nominal beam diameter 1 μm. Counting time for one spot analysis was 20 s per peak. Standards (element) are barite (S and Ba), corundum (Al), wollastonite (Ca and Si), magnetite (Fe), rutile (Ti), rhodonite (Mn), and jadeite (Na). The PAP routine was applied (Pouchou and Pichoir 1991) for correction of recorded raw data. Ten spot analyses were performed. The studied grain was found to be homogeneous. Chemical data are given in Supplemental[1] Table S1.

Ettringite is unstable under the electron beam, showing loss of water, which results in significantly higher concentrations for the remaining constituents. Therefore, Supplemental[1] Table S1 reports also "normalized" constituents to provide a total of 100 wt%, when combined with the H_2O content calculated on the basis of the neutron structure refinement. The empirical formula, based on 51 anions per formula unit, is

$$(Ca_{6.07}Na_{0.01})_{\Sigma 6.08}(Al_{1.95}Fe^{3+}_{0.01}Si_{0.01})_{\Sigma 1.97}(SO_4)_{2.99}(OH)_{12}\cdot 27H_2O.$$

Infrared spectroscopy

Due to the unstable character of ettringite, no polished single-crystal absorber could be prepared. Attempts to do so resulted in milky crystal slabs, which indicated loss of water. An unpolarized IR spectrum of powdered ettringite in a pressed KBr pellet was recorded in the 600–8000 cm^{-1} at a spectral resolution of 4 cm^{-1} during 32 cycles with a Bruker Vertex 70 microscope spectrometer equipped with a glow-bar source, a KBr beam-splitter, and a mid-band MCT detector. A disk of pure pressed KBr prepared under the same conditions was used as a standard. The recorded spectrum is shown in Figure 2.

Neutron diffraction experiment and structure refinement

The first set of single-crystal neutron diffraction data were collected from a large euhedral fragment of ettringite (approx. 12 mm^3) at a temperature of 20 K on the four-circle diffractometer D9 at the Institut Laue-Langevin (ILL), Grenoble. The wavelength used was 0.8403(1) Å obtained from a Cu(220) monochromator, and 1500 reflections were measured with a small two-dimensional area detector up to $2\theta_{max} = 84.6°$ and reduced to 739 unique reflections (Gatta and Fernández-Díaz 2018). The integration, background, and Lorentz factor correction of the scans were done with the program RACER (Wilkinson et al. 1988). To complete the structural information, the same crystal was placed on a closed-cycle refrigerator on the monochromatic four-circle diffractometer D19 at ILL. The wavelength used was 1.454(1) Å, provided by a flat Cu(220) monochromator at $2\theta_M = 69.91°$ take-off angle. The sample was cooled to 20 K at 2 K/min cooling rate. The measurement strategy consisted of 22 ω scans with steps of 0.07° at different χ and φ positions (Fernández-Díaz and Cañadillas-Delgado 2018); reflections up to $2\theta_{max} = 140.4°$ were collected ($\sin\theta/\lambda = 0.597$, max resolution: 0.84 Å). The Multi-Detector Acquisition Data Software (MAD) from ILL was used for data collection. Unit-cell determination [$a = 11.171(1)$ Å, $c = 21.364(1)$ Å] was done by using the PFIND and DIRAX programs, and processing of the raw data was performed using the RETREAT and RAFD19 programs (McIntyre and Stansfield 1988; Duisenberg 1992). Absorption corrections were applied using the D19ABS program (Matthewman et al. 1982). A total number of 14 771 Bragg reflections were collected, out of which 1745 reflections were unique for symmetry ($R_{int} = 0.0534$, Laue class $\bar{3}1m$). Initial structural refinements with SHELX-97 (Sheldrick 1997) showed that extinction was pronounced, but could be reasonably well accounted for by the Larson-like correction (Larson 1967). Other details of the data collections are listed in the CIF[1].

After preliminary checks about the consistency of the symmetry of the structure models previously reported and the diffraction pattern of this study, the anisotropic structure refinement was performed in the space group $P31c$ using the SHELX-97 software (Sheldrick 1997), starting from the structure model of More and Taylor (1970), without any H sites. The neutron scattering lengths of Ca, Al, S, O, and H were used according to Sears (1986). Secondary isotropic extinction effects were corrected according to Larson's formalism (1967), as implemented in the SHELXL-97 package (Sheldrick 1997). Intense negative residual peaks were found in the difference-Fourier synthesis of the nuclear density when convergence was achieved. Further cycles of refinement were then performed assigning H to these residual peaks (as hydrogen has a negative neutron scattering length). Convergence was slowly achieved, and the final least-square cycles were conducted with anisotropic displacement parameters for all the H sites. All the principal

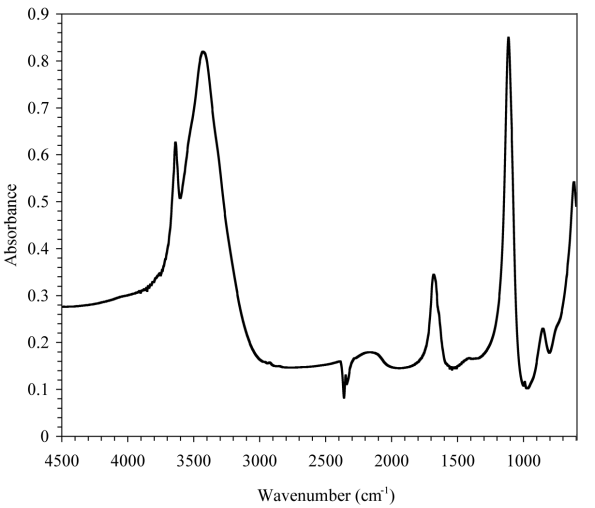

Figure 2. The infrared spectrum of ettringite.

mean-square atomic displacement parameters were positively defined. At the end of the last cycle of refinement, no peak larger than –1.2/+2.2 fm/Å^3 was present in the final difference-Fourier map of the nuclear density (maximum and minimum located near the "disordered" inter-column H_2O sites, see next session and Fig. 3) and the variance-covariance matrix showed no significant correlation among the refined parameters. The structure was refined to $R_1 = 0.0881$ using 381 refined parameters and 1664 unique reflections with $F_o > 4\sigma(F_o)$. Further details pertaining to the structure refinement (statistical parameters, fractional atomic coordinates and displacement parameters) are reported in the CIF[1]. Relevant bond lengths and angles are listed in Supplemental[1] Table S2.

Discussion and Implications

The EPMA–WDS analysis is consistent with the crystal chemistry of ettringite obtained in the previous studies, which is unusual in minerals: it contains about 47 wt% H_2O, 19 wt% SO_3, 27 wt% CaO, and 8 wt% Al_2O_3, giving a density of only ~1.83 g/cm^3. The minor content of Mn, Fe, Si, and Ti (in total <0.02 apfu, potentially replacing Al, Supplemental[1] Table S1), along with Na and Ba (in total <0.02 apfu, potentially replacing Ca, Supplemental[1] Table S1), are observed. In other words, ettringite from the N'Chwaning mine shows a composition very close to the end-member formula: $Ca_6Al_2(SO_4)_3(OH)_{12}\cdot 27H_2O$.

The neutron structure refinement based on the data collected at 20 K is consistent with the general structure model previously obtained (Moore and Taylor 1968, 1970; Goetz-Neunhoeffer and Neubauer 2006; Hartman and Berliner 2006). The present data show that all 20 crystallographically unique oxygen sites in the ettringite structure are involved in hydrogen bonding.

OW5 through OW12, OW19, and OW20 are H_2O-molecule oxygen atoms. OW5 through OW11 belong to the coordination shell of two Ca sites (i.e., Ca1: OW6, OW8, OW10, OW12; Ca2: OW5, OW7, OW9, OW11; Fig. 1, see also the CIF[1]). All the H_2O molecules are H bonded, with the following energetically favorable configurations: OW5-H3···O18 (i.e., O18 belonging to a SO_4-group), OW5-H7···O15 (i.e., O15 belonging to a SO_4-group), OW6-H1···O15, OW6-H6···O18, OW7-H12···O16 (i.e., O16 belonging to a SO_4-group), OW7-H17···OW19 (or OW20) (i.e., $H_2O\cdots H_2O$ interaction), OW8-H11···O16, OW8-H13···OW19 (or OW20), OW9-H15···O16, OW9-H16···O15, OW10-H2···O18, OW10-H20···O14 (i.e., O14 belonging to a SO_4-group), OW11-H9···OW9 (i.e., OW9 belonging to a Ca-polyhedron, $H_2O\cdots H_2O$ interaction), OW11-H19···O17 (i.e., O17 belonging to a SO_4-group), OW12-H10···O13 (i.e., O13 belonging to a SO_4-group), OW12-H18···OW10 (i.e., OW10 belonging to a Ca-polyhedron, $H_2O\cdots H_2O$ interaction), OW19-H21···OW19 (or OW20), OW19-H23···OW12 (i.e., OW12 belonging to a Ca-polyhedron, $H_2O\cdots H_2O$ interaction), OW20-H22···OW11 (i.e., OW11 belonging to a Ca-polyhedron, $H_2O\cdots H_2O$ interaction), OW20-H24···OW12 (Supplemental[1] Table S2). All the H bonds show O···O distances ranging between 2.66 and 2.98 Å (Supplemental[1] Table S2).

OH1 through OH4 are oxygen atoms of hydroxyl groups and belong to the coordination shell of the two unique Al sites (Fig. 1, see also the CIF[1]). The oxygen atoms of the hydroxyl groups act as donors, forming hydrogen-bonds with the H_2O oxygen sites (all belonging to the Ca-coordination shells) as acceptors (i.e., OH1-H8···OW5, OH2-H5···OW6, OH3-H14···OW7, and OH4-H4···OW8, Supplemental[1] Table S2). All the hydrogen-bonds show O···O distances ranging between 3.1 and 3.2 Å (Supplemental[1] Table S2).

All the building-block units of the ettringite structure [i.e., SO_4 groups, $Al(OH)_6$ octahedra and $Ca(OH)_4(H_2O)_4$ polyhedra] are connected via H bonds.

The geometry of the H_2O molecule is now well defined: the O-H distances corrected for "riding motion" (Busing and Levy

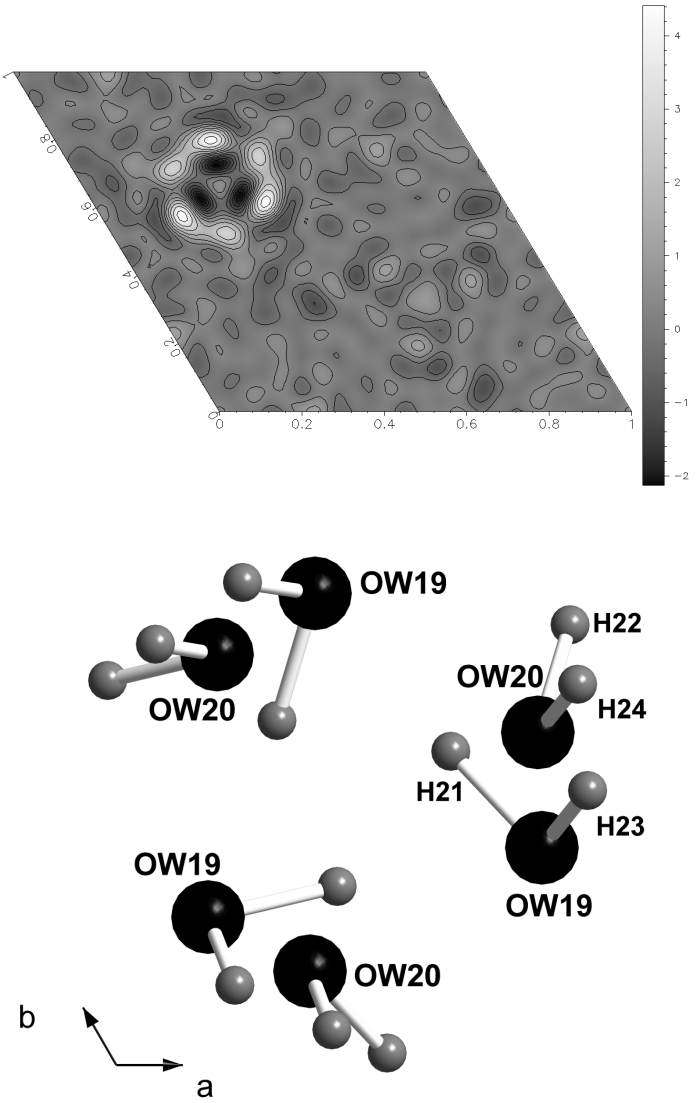

Figure 3. (**top**) Difference-Fourier maps of ettringite at $z \sim 0.235$ calculated with coefficients F_o-F_c and phased by F_c. The F_c were calculated from a structural model without the inter-column H_2O sites (H21-OW19-H23, H22-OW20-H24; CIF and Supplemental[1] Table S2). Maxima, ascribable to the missing O sites, and minima, ascribable to the missing H sites (as H has negative neutron scattering length), about the threefold axis, are visible. Color bar unit: fm/Å^3. (**down**) Schematic configuration and location of the inter-column H_2O sites.

1964) range between 0.96 and 1.07 Å (Supplemental[1] Table S2). The H-OW-H angles range between 101.7–109.7° (Supplemental[1] Table S2), and are all still in the range of the observed H-O-H angles in solid-state materials (Chiari and Ferraris 1982; Steiner 1998 and references therein; Gatta et al. 2008). For the hydroxyl groups, the O-H distances corrected for "riding motion" range between 0.94–1.02 Å (Supplemental[1] Table S2). All the hydrogen bonds show O-H···O angles ≥160° (Supplemental[1] Table S2), a configuration that is energetically less costly (i.e., approaching linearity, Steiner 1998), if compared to that of other minerals (e.g., phyllosilicates, with O-H···O angles ranging between 120–140°; Gatta et al. 2011, 2013). The oxygen and hydrogen atoms of the H_2O molecules and (OH) groups have slightly larger anisotropic displacement parameters if compared to the other sites populated by Ca, Al, or Si; the maximum ratio of the *max* and *min* root-mean-square components of the displacement ellipsoid is observed for the protons of the hydroxyl groups (i.e., OH1-OH4). However, the magnitude of the displacement ellipsoids of the non-H_2O atoms is somehow mitigated by the low *T*.

The different Fourier-map of the nuclear density shows a disordered distribution of the inter-column "free" H_2O molecules of the ettringite structure, which was modeled (in the structure refinement) with two independent and mutually exclusive configurations: H21-OW19-H23 and H22-OW20-H24 (Fig. 3, see also the CIF[1]). In the structure refinement, the best fit was obtained with s.o.f. of 0.48(1) and 0.52(1) for each configuration (then fixed to 0.5 for each one in the last cycles of refinement), leading to a total number of 27 H_2O molecules p.f.u. OW19 and OW20 act as "inter-column bridges," between the Ca-polyhedra (Supplemental[1] Table S2). As the disorder is still preserved down to 20 K, we are inclined to consider that as a "static disorder." We cannot exclude that the hydrogen-bonding network of the H_2O molecules promotes the disorder, at least partially: for each of the two configurations (i.e., OW19 and OW20), one of the two protons has an almost ideal hydrogen-bonding geometry, the other one not (i.e., with OW-H···O ranging between 162–170° vs. 144–147°, Supplemental[1] Table S2). The refined isotropic displacement parameters of the inter-column H_2O sites are likely affected by the positional disorder (presumably overestimated; see the CIF[1]). With the disordered configuration here observed, there is no domain of the structure without the presence of inter-column H_2O molecules, and thus we cannot expect a relevant role of the disorder on the stability of the structure under non-ambient conditions. Furthermore, ettringite with less than 27 H_2O molecules p.f.u., if it exists, would behave differently at non-ambient conditions.

The structure refinement shows that, in the ettringite structure, the SO_4 tetrahedra are slightly distorted, with $\Delta(S\text{-}O)_{max}$ ~0.015 Å (i.e., the difference between the longest and the shortest bond distances), and the $\Delta(O\text{-}S\text{-}O)_{max}$ ~1.5° (i.e., the difference between the highest and the lowest intra-tetrahedral angle). The $Al(OH)_6$ octahedra are more distorted, with $\Delta(Al1\text{-}O)_{max}$ and $\Delta(Al2\text{-}O)_{max}$ ~0.045 Å. The $Ca(OH)_4(H_2O)_4$ polyhedra are highly distorted, with $\Delta(Ca1\text{-}O)_{max}$ ~0.217 Å and $\Delta(Ca2\text{-}O)_{max}$ ~0.283 Å (Supplemental[1] Table S2).

The recorded infrared spectrum of ettringite (Fig. 2) shows an intense and broad absorption in the range 3150–3750 cm^{-1} with a maximum at 3427 cm^{-1}. This feature is overprinted by a relatively narrow band at 3638 cm^{-1}. In accordance with the detailed experimental and theoretical analysis of the ettringite vibrational spectra by Scholtzova et al. (2015), the broad absorption feature is assigned to O-H stretching in H_2O, while the narrow band at higher wavenumbers is ascribed to O-H stretching modes in (OH)-groups from the $Al(OH)_6$-octahedra. Absorption at 1640 and 1680 cm^{-1} are caused by bending modes in H_2O. In addition, several absorption bands are observed at lower wavenumbers (i.e., 620, 755, 855, 990, and 1114 cm^{-1}). The recorded spectrum is similar to those previously reported (e.g., Frost et al. 2013; Scholtzova et al. 2015). The assignment of the observed bands, based on the work by Scholtzova et al. (2015), is summarized in Supplemental[1] Table S3. The splitting of the H-O-H bending mode was explained by Scholtzova et al. (2015) by the presence of the "non-equivalent" H_2O molecules in the crystal structure, which is related to different hydrogen bond strength and different structural environment. Typical absorption bands in the range 1200–1250 cm^{-1} caused by $B(OH)_4$-groups in ettringite group minerals (Chukanov and Chervonnyi 2016) are not observed in the spectrum of the present sample.

Diffraction and spectroscopic findings of this study suggest that the structural stability of ettringite is mainly governed by the hydrogen-bonding geometry, as all of the major building units [i.e., SO_4, $Al(OH)_6$, Ca-polyhedra] are held together by hydrogen bonds. Similar findings were reported for thaumasite (Gatta et al. 2012). This can explain the modest stability of ettringite at high temperature (with structure collapsing at $T <$ 150 °C; Zhou and Glasser 2001) or at high pressure (evidence of amorphization were observed at P ~3 GPa; Clark et al. 2008), likely reflecting the incapacity of the hydrogen-bonding scheme to be preserved even at modest high-temperature/high-pressure conditions. In contrast, low *T* stabilizes the ettringite structure, as corroborated by the hydrogen-bonding configuration, similarly to what already observed for thaumasite (Gatta et al. 2012). We can then extend even to ettringite the same considerations reported by Gatta et al. (2012) on thaumasite: pronounced sulfate attack of Portland cement, observed in cold regions, takes place likely in response to favorable nucleation and growth of ettringite and thaumasite under such conditions. However, whereas the sulfate attack of cement promoted by percolation of sulfate-rich fluids can be potentially mitigated, by isolating the cement structures, it is difficult to prevent the delayed formation of ettringite and thaumasite promoted by the chemical components that already occur in cement paste.

We expect that the revised structural model and formula, here obtained, will be employed for more efficient identification and quantification of ettringite in polyphasic mixtures such as Portland cement. In addition, as the ettringite crystal morphology was observed to affect the expansion of cement structures (Tosun and Baradan 2010), the structure model here derived would deliver a valuable contribution to investigating any potential correlation between the ettringite's habit and its crystal structure, for example via periodic-bond-chain development (e.g., Hartman and Chan 1993).

Acknowledgments

The authors thank the Institut Laue-Langevin, Grenoble (France), for the allocation of neutron beam time. The Editor, Ian Swainson, and four anonymous reviewers are thanked. G.D.G. acknowledge the support of the Italian Ministry of Education (MIUR) through the project "Dipartimenti di Eccellenza 2018–2022."

F. Chiaravalli and G. Ventura (SOGIN, Italy) are thanked for further discussions about the durability of Portland cement in nuclear waste disposal.

References cited

Asamoto, S., Murano, K., Kurashige, I., and Nanayakkara, A. (2017) Effect of carbonate ions on delayed ettringite formation. Construction and Building Materials, 147, 221–226.

Barnett, S.J., Adam, C.D., and Jackson, A.R.W. (2000) Solid solutions between ettringite, $Ca_6Al_2(SO_4)_3(OH)_{12}\cdot 26H_2O$, and thaumasite $Ca_3SiSO_4CO_3(OH)_6\cdot 12H_2O$. Journal of Material Science, 35, 4109–4114.

Bensted, J. (1999) Thaumasite—background and nature in deterioration of cements, mortars and concretes. Cement and Concrete Composites, 21, 117–121.

Busing, W.R., and Levy, H.A. (1964) The effect of thermal motion on the estimation of bond lengths from diffraction measurements. Acta Crystallographica, 17, 142–146.

Chiari, G., and Ferraris, G. (1982) The water molecules in crystalline hydrates studied by neutron diffraction. Acta Crystallographica B, 38, 2331–2341.

Chukanov, N.V. and Chervonnyi, A.D. (2016) Infrared Spectroscopy of Minerals and Related Compounds. Springer.

Clark, S.M., Colas, B., Kunz, M., Speziale, S., and Monteiro, P.J.M. (2008) Effect of pressure on the crystal structure of ettringite. Cement and Concrete Research, 38, 19–26.

Crammond, N.J. (1985) Thaumasite in failed cement mortars and renders from exposed brickwork. Cement Concrete Research, 15, 1039–1050.

Deb, S.K., Manghnani, M.H., Ross, K., Livingston, R.A., and Monteiro, P.J.M. (2003) Raman scattering and X-ray diffraction study of the thermal decomposition of an ettringite-group crystal. Physics and Chemistry of Minerals, 30, 31–38.

Duisenberg, A.J.M. (1992) Indexing in single-crystal diffractometry with an obstinate list of reflections. Journal of Applied Crystallography, 25, 92–96.

Fernández-Díaz, M.T., and Cañadillas-Delgado, L. (2018) Structure of ettringite; Experimental Report. Institut Laue-Langevin (ILL), Grenoble. Internal DOI: 10.5291/ILL-DATA.TEST-2828.

Frost, R.L., López, A., Xi, Y., Scholz, R., Magela da Costa, G., Fernandes Lima, R.M., and Granja, A. (2013) The spectroscopic characterization of the sulphate mineral ettringite from Kuruman manganese deposits, South Africa. Vibrational Spectroscopy, 68, 266–271.

Gatta, G.D., and Fernández-Díaz, M.T. (2018) New insight into the crystal structure of ettringite: $Ca_6[Al(OH)_6]_2(SO4)_3\cdot 26H_2O$; Experimental Report. Institut Laue-Langevin (ILL), Grenoble. DOI: 10.5291/ILL-DATA.5-11-419.

Gatta, G.D., Rotiroti, N., McIntyre, G.J., Guastoni, A., and Nestola, F. (2008) New insights into the crystal chemistry of epididymite and eudidymite from Malosa, Malawi: a single-crystal neutron diffraction study. American Mineralogist, 93, 1158–1165.

Gatta, G.D., McIntyre, G.J., Sassi, R., Rotiroti, N., and Pavese, A. (2011) Hydrogen-bond and cation partitioning in $2M_1$-muscovite: A single-crystal neutron-diffraction study at 295 and 20 K. American Mineralogist, 96, 34–41.

Gatta, G.D., McIntyre, G.J., Swanson, G.J., and Jacobsen, S.D. (2012) Minerals in cement chemistry: a single-crystal neutron diffraction and Raman spectroscopic study of thaumasite, $Ca_3Si(OH)_6(CO_3)(SO_4)\cdot 12H_2O$. American Mineralogist, 97, 1060–1069.

Gatta, G.D., Merlini, M., Valdrè, G., Liermann, H-P., Nénert, G., Rothkirch, A., Kahlenberg, V., and Pavese, A. (2013) On the crystal structure and compressional behaviour of talc: a mineral of interest in petrology and material science. Physics and Chemistry of Minerals, 40, 145–156.

Goetz-Neunhoeffer, F., and Neubauer, J. (2006) Refined ettringite ($Ca_6Al_2(SO_4)_3(OH)_{12}\cdot 26H_2O$) structure for quantitative X-ray diffraction analysis. Powder Diffraction, 21, 4–11.

Hartman, M.R., and Berliner, R. (2006) Investigation of the structure of ettringite by time-of-flight neutron powder diffraction techniques. Cement and Concrete Research, 36, 364–370.

Hartman, M.R., Brady, S.K., Berliner, R., and Conradi, M.S. (2006) The evolution of structural changes in ettringite during thermal decomposition. Journal of Solid State Chemistry, 179, 1259–1272.

Hartman, P., and Chan, H-K. (1993) Application of the Periodic Bond Chain (PBC) theory and attachment energy consideration to derive the crystal morphology of Hexamethylmelamine. Pharmaceutical Research, 10, 1052–1058.

Hartshorn, S.A., Sharp, J.H., and Swamy, R.N. (1999) Thaumasite formation in Portland limestone cement pastes. Cement Concrete Research, 29, 1331–1340.

Hobbs, D.W., and Taylor, M.G. (2000) Nature of the thaumasite sulphate attack mechanism in field concrete. Cement and Concrete Research, 30, 529–533.

Larson, A.C. (1967) Inclusion of secondary extinction in least-squares calculations. Acta Crystallographica, 23, 664–665.

Manzano, H., Ayuela, A., Telesca, A., Monteiro, P.J.M., and Dolado, J.S. (2012) Ettringite strengthening at high pressures induced by the densification of the hydrogen bond network. Journal of Physical Chemistry C, 116, 16138–16143.

Matthewman, J.C., Thompson, P., and Brown, P.J. (1982) The Cambridge Crystallography Subroutine Library. Journal of Applied Crystallography, 15, 167–173.

McIntyre, G.J., and Stansfield, R.F.D. (1988) A general Lorentz correction for single-crystal diffractometers. Acta Crystallographica A, 44, 257–262.

Moore, A., and Taylor, H.F.W. (1968) Crystal structure of ettringite. Nature, 218, 1048–1049.

——— (1970) Crystal structure of ettringite. Acta Crystallographica B, 26, 386–393.

Pouchou, J.L., and Pichoir, F. (1991) Quantitative Analysis of Homogeneous or Stratified Microvolumes Applying the Model "PAP". In Heinrich, K.F.J. and Newbury, D.E., Eds., Electron Probe Quantification, p. 31–75. Plenum Press, New York.

Renaudin, G., Sengi, R., Mentel, D., Nedelec, J.M., Leroux, F., and Taviot-Gueho, C. (2007) A Raman study of the sulfated cement hydrates: ettringite and monosulfoaluminate. Journal of Advanced Concrete Technology, 5, 299–312.

Renaudin, G., Filinchuk, Y., Neubauer, J., Goetz-Neunhoeffer, F. (2010) A comparative structural study of wet and dried ettringite. Cement and Concrete Research, 40, 370–375.

Santhanam, M., Cohen, M.D., and Olek, J. (2001) Sulfate attack research—wither now? Cement and Concrete Research, 31, 845–851.

Scholtzová, E., Kucková, L., Kožíšek, J., and Tunega, D. (2015) Structural and spectroscopic characterization of ettringite mineral—combined DFT and experimental study. Journal of Molecular Structure, 1100, 215–224.

Sears, V.F. (1986) Neutron Scattering Lengths and Cross-Sections. In K. Sköld and D.L. Price, Eds., Neutron Scattering, Methods of Experimental Physics, vol. 23A, p. 521–550. Academic Press, New York.

Sheldrick, G.M. (1997) SHELX-97. Programs for crystal structure determination and refinement. University of Göttingen, Germany.

Skoblinskaya, N.N., and Krasilnikov, K.G. (1975) Changes in crystal structure of ettringite on dehydration. Part 1. Cements and Concretes Research, 5, 381–394.

Skoblinskaya, N.N., Krasilnikov, K.G., Nikitina, L.V., and Varlamov, V.P. (1975) Changes in crystal structure of ettringite on dehydration. Part 2. Cement and Concrete Research, 5, 419–432.

Speziale, S., Jiang, F., Mao, Z., Monteiro, P.J.M., Wenk, H-R., Duffy, T.S., and Schilling, F.R. (2008) Single-crystal elastic constants of natural ettringite. Cement and Concrete Research, 38, 885–889.

Steiner, T. (1998) Opening and narrowing of the water H-O-H angle by hydrogen-bonding effects: Re-inspection of neutron diffraction data. Acta Crystallographica B, 54, 464–470.

Taylor, H.F.W. (1997) Cement Chemistry, 2nd ed., Thomas Telford, London.

Tosun, K., and Baradan, B. (2010) Effect of ettringite morphology on DEF-related expansion. Cement and Concrete Composites, 32, 271–280.

Wilkinson, C., Khamis, H.W., Stansfield, R.F.D., and McIntyre, G.J. (1988) Integration of single-crystal reflections using area multidetectors. Journal of Applied Crystallography, 21, 471–478.

Zhang, F.C., Ma, B.G., Yin, G., Wu, Y.Y., and Zhu, Y.C. (2009) Preparation and performance of sulfate resistance cement-based material. Key Engineering Materials, 400, 195–201.

Zhou, Q., and Glasser, F.P. (2001) Thermal Stability and Decomposition Mechanisms of Ettringite at <120°C. Cement and Concrete Research, 31, 1333–1339.

Manuscript received August 18, 2018
Manuscript accepted September 20, 2018
Manuscript handled by Ian Swainson

Endnote:

[1]Deposit item AM-19-16783, CIF and three tables. Deposit items are free to all readers and found on the MSA website, via the specific issue's Table of Contents (go to http://www.minsocam.org/MSA/AmMin/TOC/2019/Jan2019_data/Jan2019_data.html).